JOURNAL OF MATERIALS SCIENCE **25** (1990) 2149–2158

Electron microscopy study of mesophase pitch-based graphite fibres

E. J. ROCHE
E. I. DuPont de Nemours and Co., Central Research and Development Department, Experimental Station, PO Box 80356, Wilmington, Delaware 19880-0356, USA

A comprehensive electron microscopic investigation of the structure of the graphitic sheet in mesophase pitch-based fibres is presented. *In situ* brightfield and (0 0 *l*) darkfield observation of the sheets in sub micrometre fibres reveals a finely striated structure, associated with three-dimensional order. (*h k l*) darkfield imaging of the sheets in their edge-on and face-on orientations indicates that the striations correspond to the edge view of a mosaic of graphite grains. The grains have lateral dimensions of 100 to 200 nm on average but are only a few atomic layers thick. *In situ* lattice imaging of the fibre edges indicates a very high level of lattice perfection of the (0 0 *l*) domains below the fibre surface, quite in line with the outstanding mechanical and thermal properties of this type of fibres. A variety of surface defects are revealed. Preferential orientation effects of the sheet texture on the fibre electron diffraction pattern are described.

1. Introduction

Transmission electron microscopy (TEM) has been instrumental in providing an understanding of the structure of carbon fibres, now the fibres of choice in most high performance composite structures [1]. Recent studies have been mainly concerned with the fibres which have captured the largest market share, i.e. fibres from PAN precursor [2–4]. Because of their later development [5], detailed investigations of mesophase pitch-based fibres are just beginning to appear. A well marked sheet-like morphology, easily detected by scanning electron microscopy (SEM), characterizes these fibres [4–6]. This morphology, traced back to the parent carbonaceous mesophase [7, 8], favours the alignment of the graphitic layers. As a result, Young's moduli approaching the theoretical value of single crystal graphite have been reported [9]. Arrangement of the sheets into a variety of textures has been described and their relationship to strength discussed [10, 11]. In a recent electron microscopy study of a series of commercially available fibres [12], Endo proposed that the degree of folding of the sheets correlates with fibre strength; a parallel was drawn between the folded morphology of the high strength fibres and the model of Guigon *et al.* [3] for PAN-based fibres. Planarity of the sheets was found characteristic of the high modulus, graphitized, fibres.

The present paper complements a preliminary report describing the mosaic nature of the graphitic sheet [13]. A comprehensive TEM analysis of ultra-fine graphite fibres by means of electron diffraction, multiple-mode darkfield imaging and (0 0 2) lattice imaging is provided. *In situ* characterization of the structure is stressed. *In situ* observation presents many advantages, particularly the elimination of artefact inherent to any specimen thinning technique. It was reported as early as 1960 for graphite whiskers grown in a d.c. arc [14] and, more recently, for the detection of internal flaws in PAN-based fibres of a conventional size [15]. High voltage was required in this case to provide the necessary beam penetration. Such an approach is of limited application because of severe chromatic aberration and superposition effects. The fibres described in the present study were thin enough to allow high resolution observation of the structure at conventional voltages, while still representative of fibres of a much larger diameter.

2. Experimental details

The fibres were spun from a mesophase petroleum pitch by a proprietary method and heat treated through the various temperature cycles in the usual way [16] to a graphitization temperature of about 2500° C. The fibres had diameters in the 3 to 8 μm range but a few fibres were obtained which were much finer. SEM micrographs of representative fibres are shown in Fig. 1. The familiar sheet-like texture typical of mesophase pitch-based fibres is observed. Fibres with a diameter of 2 μm or less could be directly examined by TEM. However, the centre portion of the fibre could be usefully imaged for diameters of no more than about 0.5 μm. For complementary observation, fibres were also fragmented with mortar and pesle. Specimens were floated on water and picked up on carbon coated grids.

A JEOL 2000 EX transmission electron microscope, operated at 200 kV and equipped with a Gatan model 622 TV system, was used. For symmetrical (0 0 2) lattice imaging, a 8.0 nm^{-1} objective aperture was used. The objective lens focus was then adjusted to about −80.0 nm; this value corresponds to the optimum imaging conditions for a 1.9 mm C_s pole

0022-2461/90 $03.00 + .12

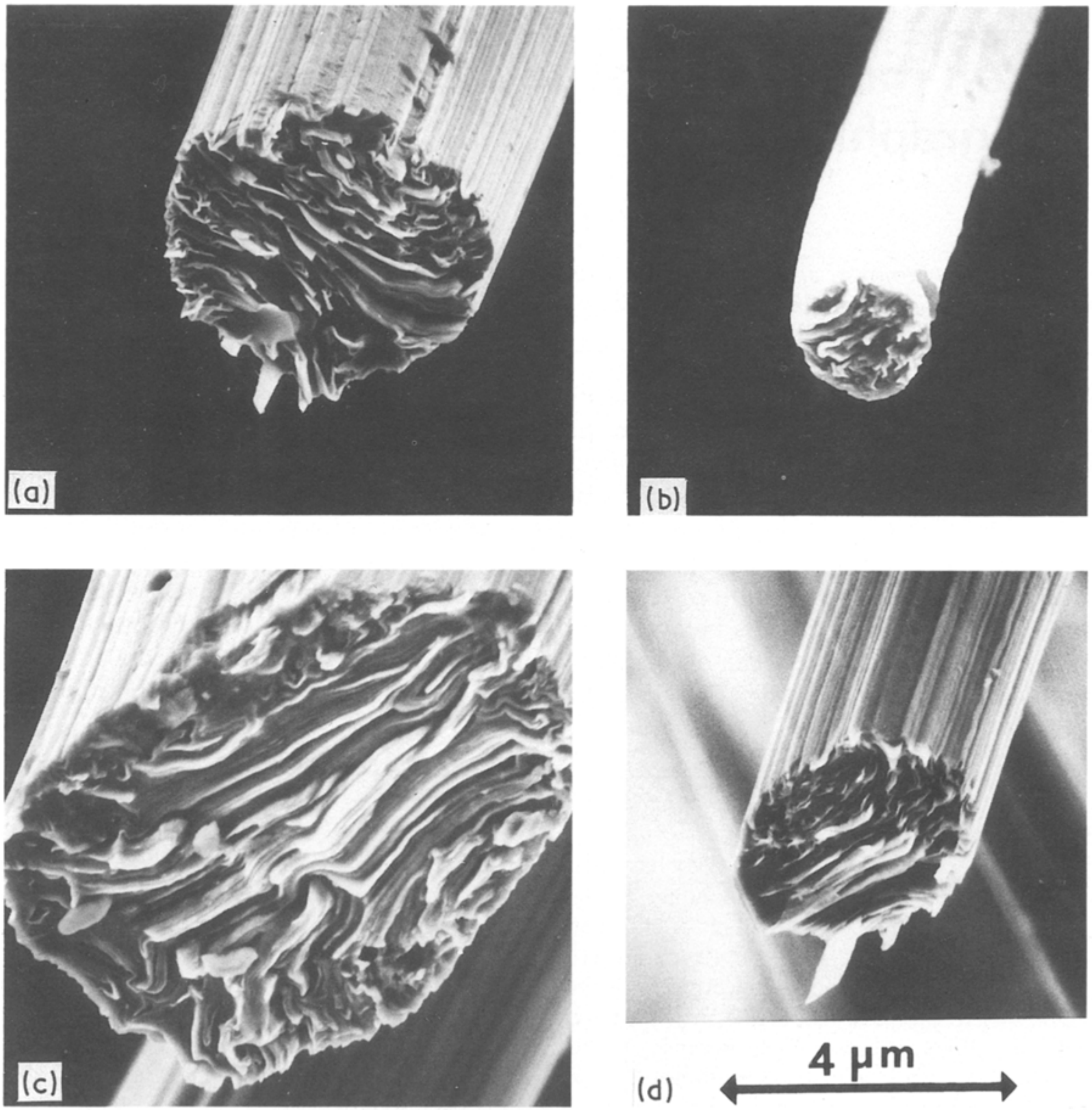

Figure 1 SEM micrographs showing the sheet texture of the fibres.

piece and 200 kV electrons; Fig. 2 shows the corresponding contrast transfer function up to the aperture spatial frequency cut-off. Darkfield imaging was performed in the tilted beam mode with objective apertures of 1.2 and 3.5 nm^{-1} effective size. The focus was then adjusted closer to zero defocus value to minimize the phase shift across the aperture [17]. The effective size of the apertures determines the resolution of the darkfield micrographs, about 0.8 and 0.5 nm, respectively, in this case. The same small apertures were used for contrasted brightfield imaging (all diffracted beams excluded). Electron diffraction patterns were recorded in proper orientation with respect to the image by double exposure. When appropriate, the area selected for diffraction was also recorded by the same method. Kodak SO-163 film was used.

SEM micrographs were obtained from uncoated specimens with a Hitachi S-800 instrument operated at 3.0 kV.

3. Electron diffraction by polycrystalline graphite

Application of transmission electron microscopy to carbon has been reviewed before [18–20]. Of special interest here is Oberlin's analysis of darkfield contrast mechanisms [20]. To facilitate the discussion of our results, it is briefly reviewed below and expanded to include the effect of preferential texture orientation on the fibre diffraction pattern.

3.1. Diffraction by turbostratic layers

Electron diffraction by a single graphite crystal is considered first*. Selected orientations of this ideal graphite crystal leading to diffraction of the electron beam (diffraction occurs if a family of planes is nearly parallel to the incident beam) are illustrated in Fig 3. In Fig. 3a, the electron beam is perpendicular to the face of the aromatic layers; $(h\,0\,0)$ and $(h\,k\,0)$ planes diffract and give rise to an hexagonal pattern (Fig. 3d).

---

*The structure described in "JCPDS, #25-284" (International Centre for Diffraction Data, Swarthmore PA, USA) lists spacings very close to our data; it has hexagonal symmetry (space group: P63mc). A cubic shape is used in the schematic in Fig. 3 for simplicity.

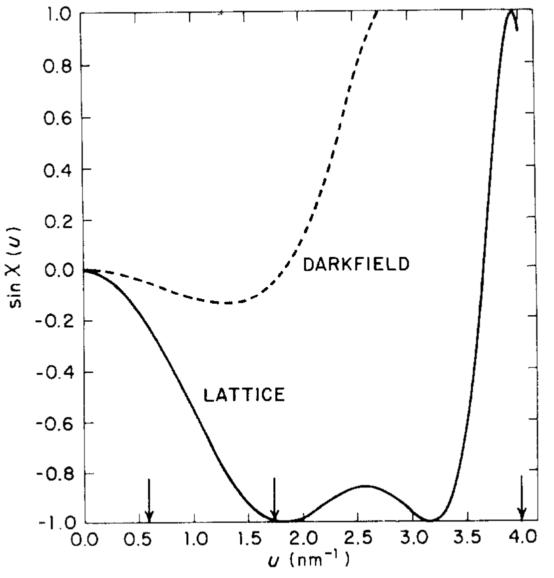

Figure 2 Contrast transfer function for lattice (——) and darkfield (- - -) imaging; the arrows indicate the various aperture cut-offs.

This basal plane orientation is the one most accessible for single crystal graphite and has been thoroughly characterized [21]. In Figs 3b and c, the beam glances off the aromatic layers and $(0\,0\,l)$ diffraction results. At the same time, $(1\,0\,l)$ or $(1\,1\,l)$ additional reflections may occur (Figs 3e and f, respectively) for proper orientation of the crystal about an axis perpendicular to the aromatic layer plane. Higher order reflections are not represented in the figure.

For turbostratic layers, the diffraction conditions are relaxed in a familiar way. Following Oberlin's analysis [20], this is best explained with the help of the Ewald construction, as represented in Fig. 4. Reciprocal (1 0) and (1 1) nodes are extended into spikes arranged along cylinders with axis perpendicular to the fibre axis. Because of the small crystal size, the spikes are not resolved. Figures 4a to c show, respectively, the layers in direct space, the Ewald construction and the resulting diffraction pattern, for a "face-on" orientation. The diffraction pattern is given by the intersection of the cylinders with the Ewald sphere (which approximates to a plane). Because of the fine mosaic, diffraction rings are obtained in place of the single crystal reflections shown in Fig. 3d.

As the layer tilts about the fibre axis (Fig. 3d to f), the long cylinders still intersect the Ewald sphere, but now define ellipses rather than circles. Finally, as the layers reach an "edge-on" orientation, the ellipses become lines (Fig. 3g to i). At the same time $(0\,0\,l)$ reflections appear.

3.2. Diffraction by a graphitic mosaic

The specimen is now a thin sheet built up of large (in the plane of the sheet) graphite grains, as represented in Figs. 5a. In the reciprocal space (Fig. 5b), the $(h\,k\,l)$ nodes are still arranged cylindrically, but the presence of three-dimensional order is expressed by the modulation of the diffracted intensity along the spikes. Also, because of the large lateral size of the grains, the spikes are resolved. The continuous cylinders of Fig. 4 are therefore replaced by layers of cylindrically arranged short rods (Fig. 5b). For the face-on orientation, the only noticeable change from the turbostratic case is the resolution of the (1 0 0) and (1 1 0) rings of the diffraction pattern into discrete spots (Fig. 5c). As the mosaic begins to tilt, the (1 0 0) and (1 1 0) rods still intersect the Ewald sphere, but along an ellipse (Fig. 5d to f). As the mosaic tilts further, rods of higher l index also intersect the sphere, as illustrated in Figs 5g to h. The ellipticity of the pattern increases and the intensity distribution becomes modulated, with $(1\,0\,l)$ and $(1\,1\,l)$ reflections appearing on the inside and outside ellipses, respectively (Fig. 5i).

Finally, in the case of the edge-on orientation (Figs 5j to l), some rods only will intercept the Ewald sphere, but now along their longest dimension. This results in the streaky appearance of the corresponding $(h\,k\,l)$ reflections, now arranged along layer lines. $(0\,0\,l)$ reflections are observed at the same time. These reflections have a more isotropic shape because of the much larger size of the corresponding coherent domains. While all grains of the mosaic contribute to $(0\,0\,l)$ reflections, each may contribute to either the $(1\,0\,l)$ or the $(1\,1\,l)$ lines (and higher orders) or neither, depending on the in-plane orientation of the aromatic structure.

Darkfield imaging provides projection views of the crystals corresponding to the selected diffraction spot. Selection of $(h\,k\,0)$ or $(h\,k\,l)$ reflections from patterns

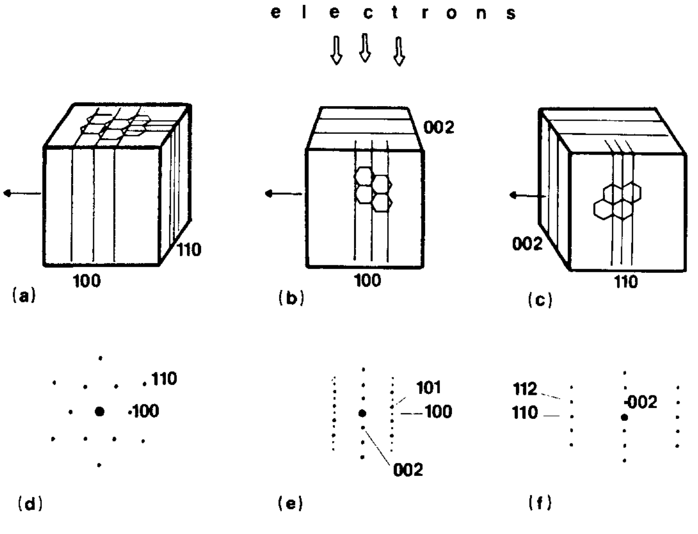

Figure 3 Relevant orientations of a graphite crystal about the fibre axis (arrow) and corresponding diffraction patterns; the cubic shape is used for simplicity only. (a, d) face-on orientation; (b, e) and (c, f) edge-on orientations.

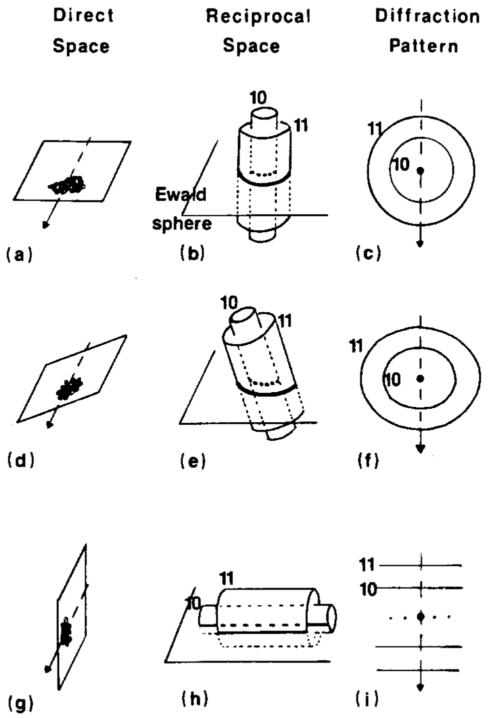

Figure 4 Ewald construction for a turbostratic layer; electron beam is vertical, arrows indicate the fibre axis. (a–c) face-on, (d–f) tilted, (g–i) edge-on orientations.

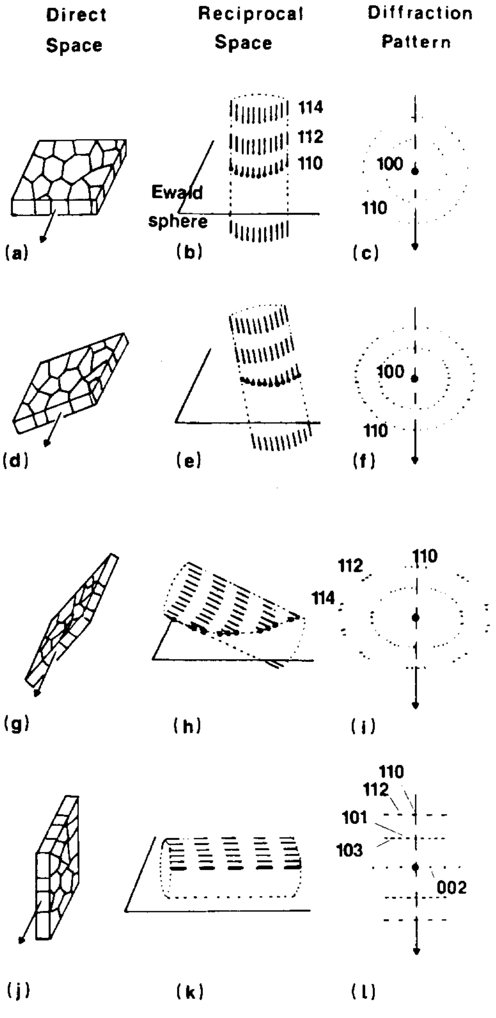

Figure 5 Ewald construction for a graphitic mosaic; electron beam is vertical, arrows indicate the fibre axis. (a–c) face-on, (d–f) and (g–i) tilted, (j–l) edge-on orientations. Intersection of the Ewald sphere and reciprocal lattice is indicated by thicker lines.

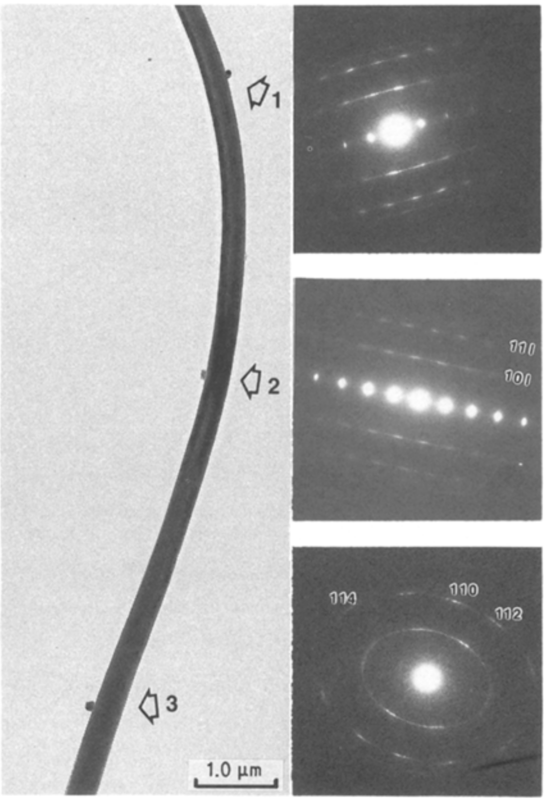

Figure 6 Low magnification brightfield micrograph of a twisting fibre and corresponding electron diffraction patterns recorded from the regions indicated by arrows. Size of diffraction area is shown in Fig. 8.

such as those in Figs 5c, f, i, or l will therefore provide images of, respectively, face-on, tilted or edge-on grains. For the edge-on orientation, $(0\,0\,l)$ darkfield will image the whole edge of the mosaic rather than individual grains.

4. Results and discussion

4.1. *In situ* observation of the mosaic

Figure 6 shows a brightfield electron micrograph and corresponding electron diffraction patterns of an ultrafine fibre, about 300 nm in diameter, which has an undulating shape resulting from the progressive axial twisting of its internal structure. This twisting is indicated by the changing features of the electron diffraction patterns recorded at three different positions along the fibre, identified by fortuitious particulate contaminants. In position "2", the electron diffraction pattern exhibits extremely intense $(0\,0\,l)$ reflections, an indication of nearly perfect edge-on orientation. This is confirmed by the straightness of the $(h\,k\,l)$ lines, quite as predicted by the schematic in Fig. 5l. As explained above, the reflections on these lines are streaky, a feature associated with the small thickness of the crystals in the direction perpendicular to the layers. Also, the $(1\,1\,l)$ lines appear better resolved because reflections with l odd are forbidden. For the $(1\,0\,l)$ lines, reflections with l even are very weak but allowed, so that the lines appear more continuous.

Towards the top of the fibre, the respective intensities of $(h\,k\,l)$ and $(0\,0\,l)$ reflections in the pattern from segment "1" are more balanced, and the $(h\,k\,l)$ reflec-

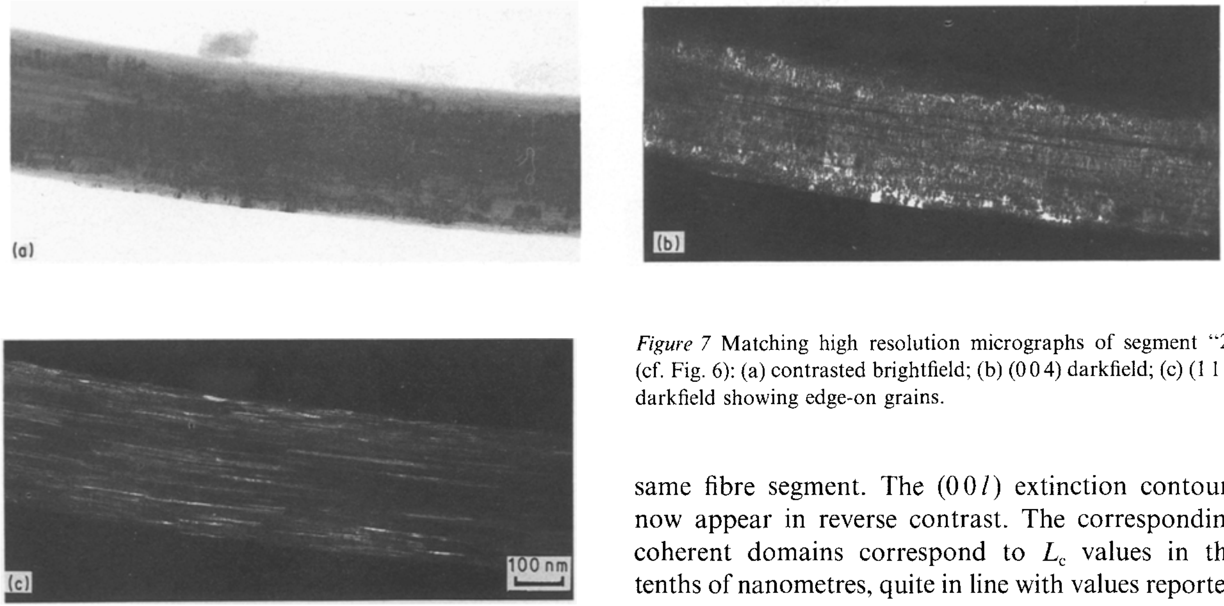

Figure 7 Matching high resolution micrographs of segment "2" (cf. Fig. 6): (a) contrasted brightfield; (b) (0 0 4) darkfield; (c) (1 1 2) darkfield showing edge-on grains.

tions exhibit some arcing. This is an indication that part of the aromatic layers begin to tilt away from the edge-on orientation. In region "3", this tilting (in the reverse direction) is much more important since $(0\,0\,l)$ reflections have totally disappeared from the diffraction pattern, now quite similar to the pattern schematized in Fig. 5i. In all patterns, the high number of higher order $(h\,k\,l)$ reflections attests to the high degree of graphitization.

The crystalline texture is now examined by darkfield imaging. Segment "2" is examined first, with the help of the micrographs in Fig 7. In the brightfield image of Fig. 7a, the dark features originate from diffraction contrast. Two types of features are noticed: the first type is of a familiar nature and consists of $(0\,0\,l)$ extinction contours; the second type consists of dark striations parallel to the fibre direction. $(0\,0\,l)$ extinction contours in carbon fibres have been documented for a long time [18]. The other feature, to our knowledge, is discussed here for the first time. Its nature can be elucidated by darkfield imaging. Figure 7b shows a typical $(0\,0\,l)$ darkfield image, (0 0 4) in this case, of the same fibre segment. The $(0\,0\,l)$ extinction contours now appear in reverse contrast. The corresponding coherent domains correspond to L_c values in the tenths of nanometres, quite in line with values reported for highly graphitized fibres [12]. Dark striations running across the contours are, however, well visible. By superposition of the corresponding negatives, they can be shown to match the dark striations in the brightfield image. Their exact origin is revealed by $(h\,k\,l)$ darkfield imaging. Figure 7c shows, for example, a (1 1 2) darkfield image of the same fibre segment. Bright elongated domains are imaged, which correspond to many of the dark striations in either of the two preceeding images. They represent edge projections of the graphite grains. The grains are only 1 to 2 nm thick. Another set of grains may be imaged by (1 0 1) darkfield imaging (see below).

Fibre segment "1" is imaged in the same conditions in Fig. 8. The brightfield image in Fig. 8a shows only one region with exact edge-on orientation (dark band along upper edge), which explains the relative weakness of the $(0\,0\,l)$ row in the corresponding diffraction pattern in Fig. 6 (the pattern was recorded from the lighter area). In the (0 0 2) darkfield image (Fig. 8b), the reverse contrast of the edge-on region is noticed, while little contrast is observed in the other regions of the fibre where the layers are inclined. Much higher contrast is obtained from the (1 1 2) darkfield image, shown in Fig. 8c. Graphite grains are imaged, seen at a slight angle. They appear to have a polygonal shape, with lateral dimensions of the order of 100 nm. In the upper edge region, as was the case for most of segment "2", the grains are imaged on their edge. A careful examination of the images indicates that some of them exhibit Bragg extinction contours, revealed in their

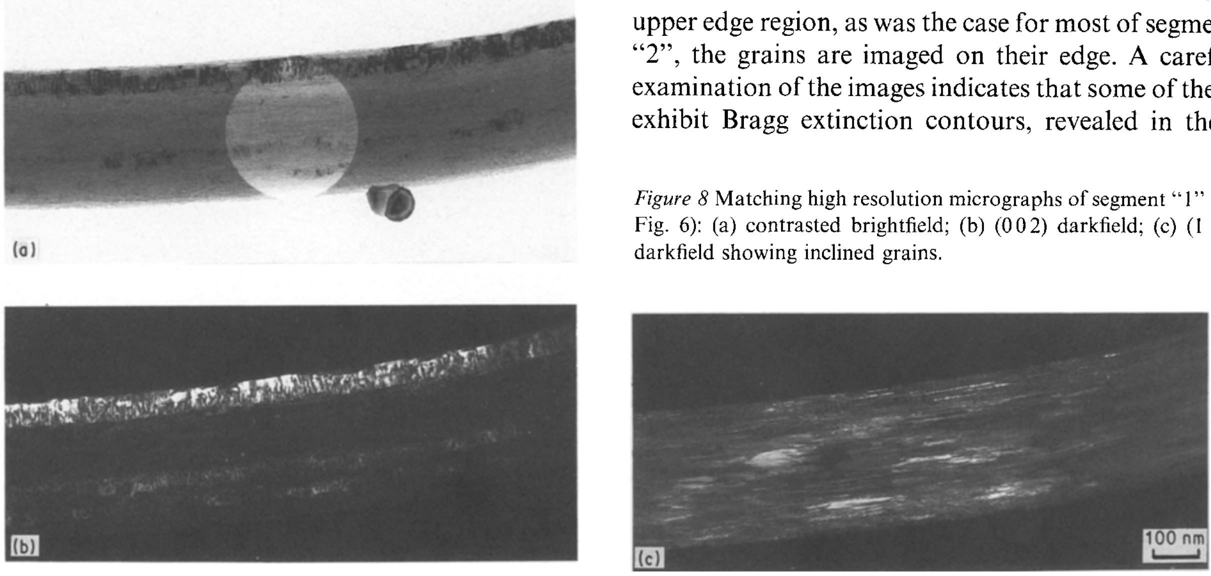

Figure 8 Matching high resolution micrographs of segment "1" (cf. Fig. 6): (a) contrasted brightfield; (b) (0 0 2) darkfield; (c) (1 1 2) darkfield showing inclined grains.

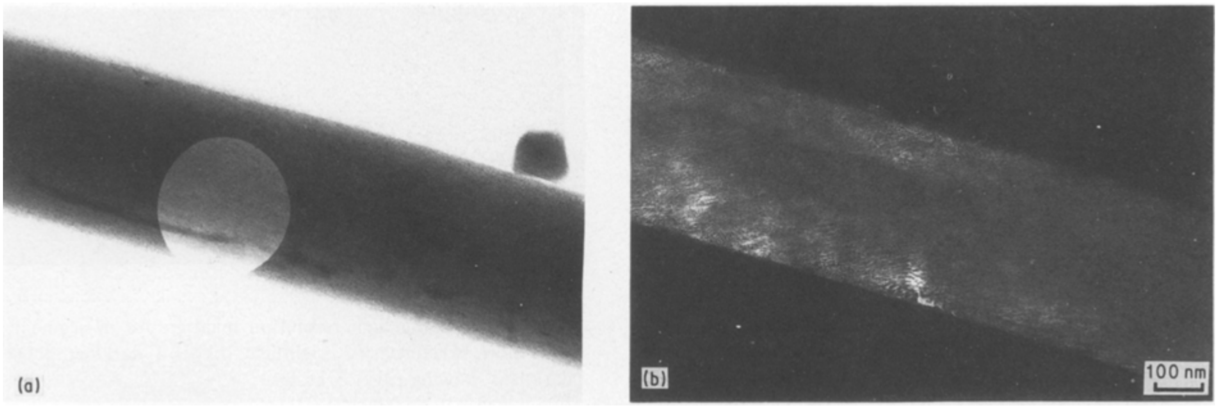

Figure 9 Matching high resolution micrograph of segment "3" (cf. Fig. 6) showing the layers in face-on orientation: (a) contrasted brightfield; (b) (1 1 2) darkfield.

dotted appearance. The fine scale of these extinction contours is explained by the small amplitude of the corresponding **g** vector[†].

Finally, segment "3" of the fibre is imaged in Fig. 9. The light, circular area in the brightfield image in Fig. 9a indicates the area selected for the diffraction shown in Fig. 6. It may be used to calibrate the fibre diameter and observe its variation between regions "1" and "3". This change may be apparent only and due to an elliptical cross section. As explained above from observation of the diffraction pattern, a nearly face-on orientation of the aromatic layers is expected. Indeed, the (1 1 2) darkfield image (Fig 9b) reveals a series of moire patterns which confirm the mosaic nature of the graphitic structure.

The emerging structure of the sheet is therefore that of a mosaic of thin graphite grains. The characteristic sizes of the grains may be obtained by a variety of imaging modes. They appear with best contrast, however, in the $(h\,k\,l)$ darkfield images. Their thickness is of the order of 1 to 2 nm only for the present fibres, while their length ($L_{a\parallel}$) ranges from 50 to 300 nm and beyond. Measurement of their width ($L_{a\perp}$) is more uncertain because of moires and other superposition effects (see below).

4.2. Observation of isolated sheets

For face-on, high resolution imaging of the mosaic, isolated sheets obtained by mild grinding of the fibres were examined. Grinding is known to induce a broadening of the (0 0 2) profile for some carbons, particularly the less graphitized ones [22]. In this study, grain size measurements in fragments were in good agreement with the *in situ* measurements, thus supporting the validity of the approach. The (1 1 0) darkfield micrograph in Fig. 10 presents a striking view of the mosaic in the form of moire patterns. Selection of the (1 1 0) rather than (1 1 2) imaging mode allows full imaging of the mosaic in spite of its twisted morphology, apparent in the narrowing grain size across the image. This morphology probably originates from a twist disclination in the pitch [7]. A cursory examination of the image may suggest that the grains have a nearly rectangular shape. This is due to the tilted orientation of the mosaic: upon careful examination of this and other micrographs, the polygonal shape of the grains appears evident. This morphology is quite similar to that encountered in graphitic films for evaporated carbon [20]. Such images can, however, lead to erroneous measurement since moire patterns are accompanied by severe truncation effects. As an illustration of the involved error, the histogram in Fig. 11 compares the grain length ($L_{a\parallel}$) estimated from the edge-on view (top left side of Fig. 10, no moires) to those from the moires. The difference in two

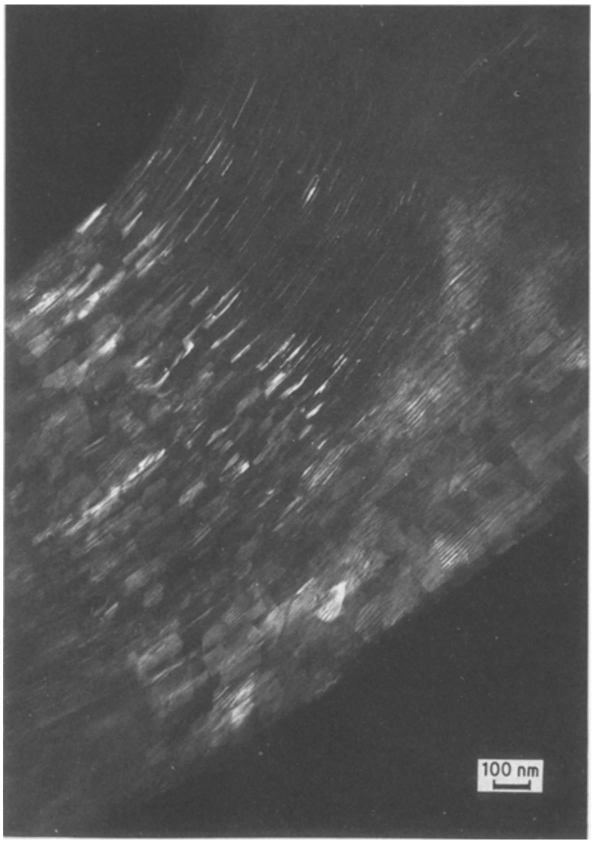

Figure 10 (1 1 0) darkfield image of a sheet fragment showing a twisted mosaic; fibre direction is SW–NE.

[†] (1 1 2) nodes are far out in the reciprocal space and intersect the Ewald sphere along their shorter dimension (their diameter see Fig. 5) they "miss" the Ewald sphere for even the most minute deviation from the exact Bragg orientation. (0 0 2) nodes are closer and "thicker".

distributions is striking, with the disappearance of the large size tail of the distribution in the latter.

Finally, the question arises of whether the entire structure is graphitized "at once", in the form of the thin mosaic layers, or some turbostratic order remains between the platelets as they progressively form with higher temperature treatment. The electron diffraction data indicates that the latter is unlikely: $(k\,k\,l)$ layer lines are resolved, up to high orders. The thickest ($2\,\mu$m) fibres may have electron diffraction patterns with continuous $(h\,k\,l)$ lines, but this is most probably an effect of the reduced resolution due to chromatic effects. Darkfield imaging supports the same interpretation. Comparison of the (1 1 0) and (1 1 2) darkfield images of the same edge-on region (Fig. 12a and b, respectively) proves the point. While the former should image both turbostratic and graphitic struc-

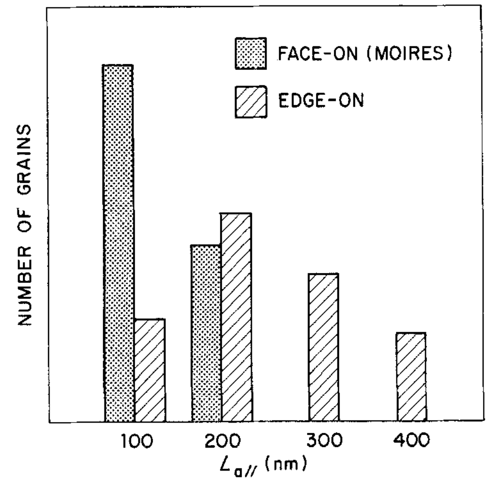

Figure 11 Comparison of the grain size distributions obtained from measurement from face-on (moires) or edge-on orientations.

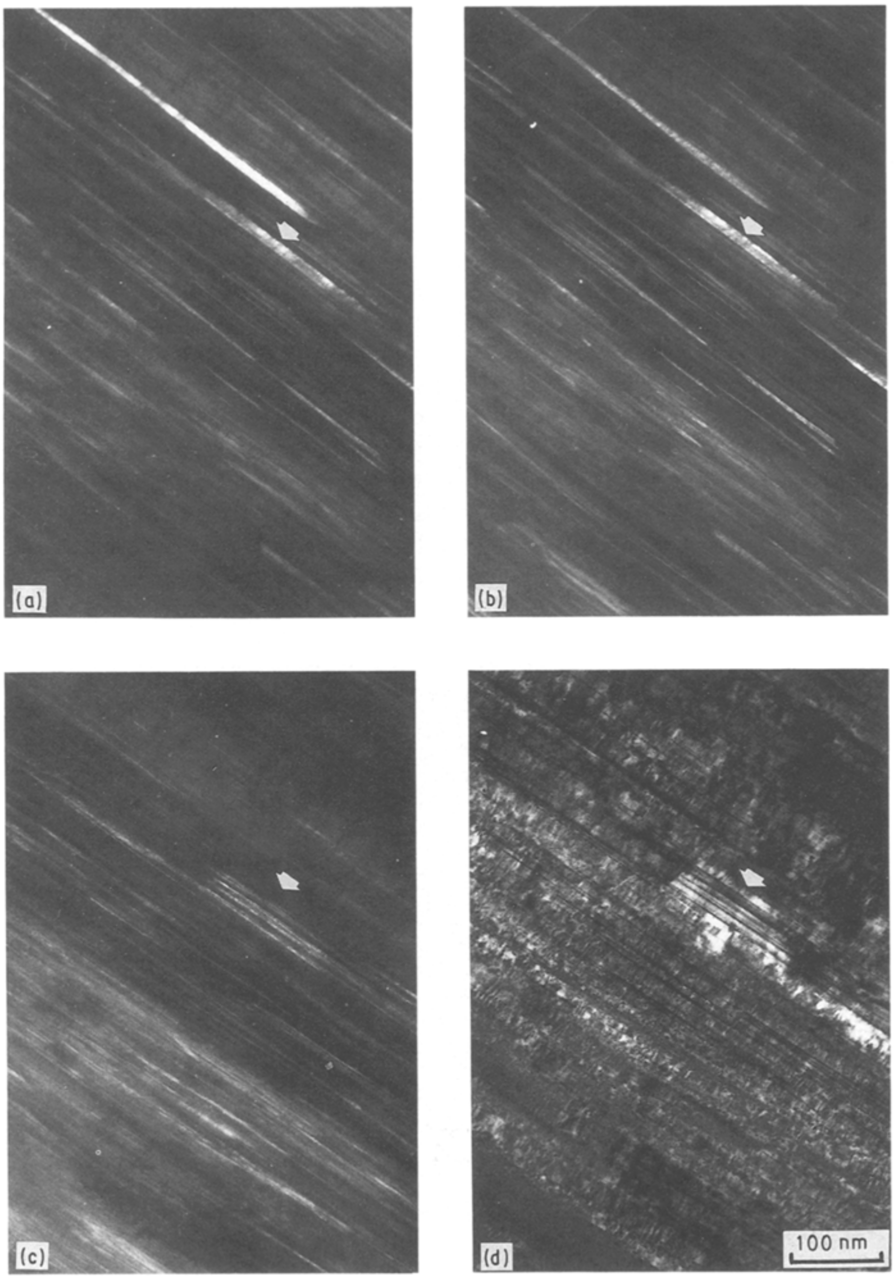

Figure 12 (a) to (d): (1 1 0), (1 1 2). (1 0 1) and (0 0 2) matching darkfield electron micrographs of a sheet fragment.

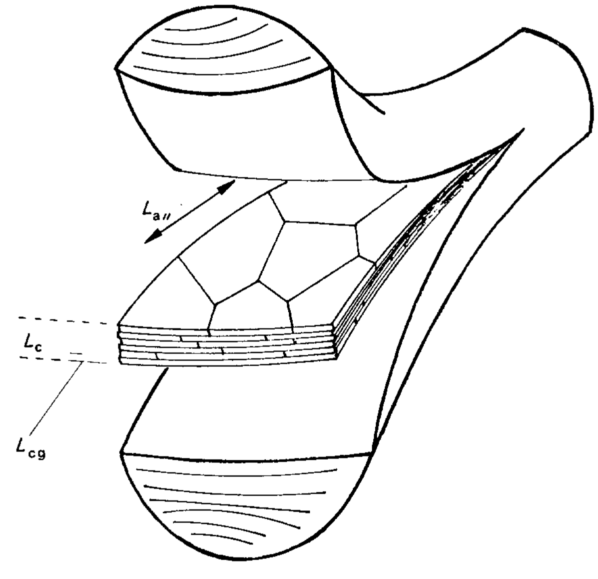

Figure 13 Schematic of the proposed sheet structure in mesophase pitch-based graphite whiskers. L_c = 30–100 nm, L_{cg} = 1–2 nm, $L_{a\parallel}$ = 50–200 nm, 2500° C graphitization.

tures, the latter should image graphitic structures only; no significant difference is, however, observed. To complete the darkfield analysis, the (1 0 1) image of the same region is shown in Fig. 12c. A totally different set of grains is imaged (use arrow for reference). Both the (1 1 *l*) and (1 0 *l*) sets are imaged simultaneously, in reverse contrast, in the (0 0 2) darkfield image in Fig. 12d. Little "free" space is left between the imaged crystals: it is reasonable to assume that all of it corresponds to grains of the mosaic in a different azimuthal orientation (in the plane of the sheet). In-plane preferential orientation effects have been recently mentioned for PAN-based and pitch-based carbon fibres [23, 24]. Such effects would result in (1 0 1) and (1 1 2) images with very different crystal densities. This question was not investigated further.

In light of these observations, a schematic of the idealized graphite whisker from mesophase pitch is proposed in Fig. 13. Common parameters used in the description of carbon structures (L_c, L_a) have been indicated. The graphite grain thickness has been noted L_{cg}. This morphology is rather different from the high strength scroll structure of whiskers grown in a d.c. arc [14]. Fibres of a conventional size generally do not have the simple sheet morphology because wrinkling of the sheets in the direction transverse to the fibre axis is quite common. This wrinkling results in a more complex diffraction pattern. An example of a well graphitized sheet fragment is shown in Fig. 14 together with its diffraction pattern. Because of the varying orientation of the graphitic layers, all possible features of the diffraction pattern, according to theoretical considerations in section 3.2. above, are observed. Notably, (1 0 0) and (1 1 0) rings and ellipses (double arrows) corresponding to face-on and slightly tilted mosaics are noticed, with the ellipses' reflections elongated in a direction perpendicular to the tilt (fibre) axis. Originating from the regions in dark contrast in the image, are the (0 0 *l*), (1 0 *l*) and (1 1 *l*) lines. The reflections on the (*h k l*) layer lines are very streaky for the reason explained earlier (thin grains). In conclusion, electron diffraction data point towards the same type of mosaic in the larger fibre, and it can indeed be imaged in similar fashion. This is the case, for example, of the commercial Thornel P100 fibres.

4.3. *In situ* (0 0 2) lattice imaging

In situ lattice imaging of the edge region of rayon-based carbon fibres was reported by Hugo *et al.* [25]. In the present work, availability of much finer fibres and improved optics have provided for a better insight into the structure. Lattice imaging of a quality at least equal to that obtained from thin sections [3, 12, 26] was found possible from the edge regions of fibres with diameter up to about 2 μm. A first example of such imaging is shown in Fig 15. The insert in the figure is a low magnification (0 0 2) darkfield image of the entire fibre where the arrow points towards the

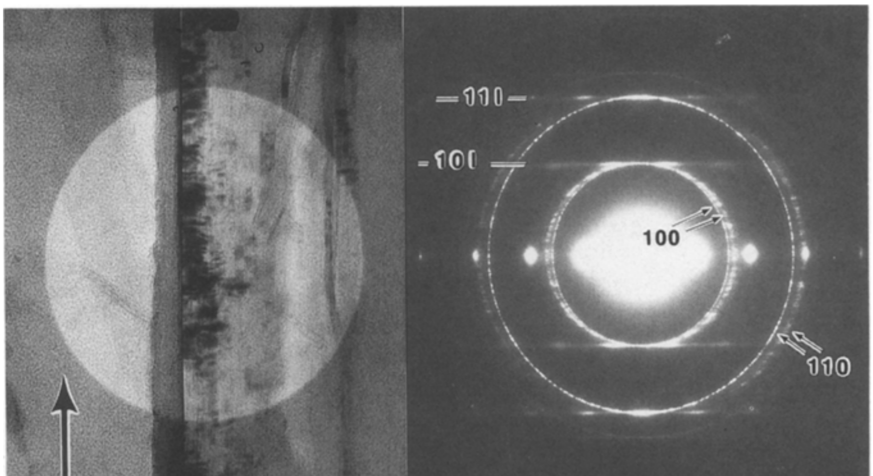

Figure 14 Contrasted brightfield micrograph of sheet fragment from a large diameter fibre and corresponding electron diffraction pattern. Arrow indicates fibre direction.

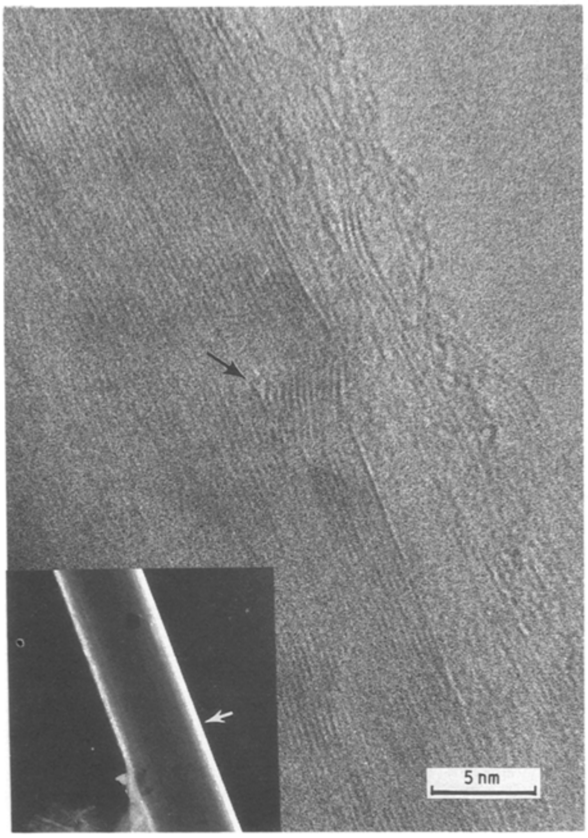

Figure 15 *in situ* (0 0 2) lattice image of a fibre edge. Inset: (0 0 2) darkfield image of complete fibre.

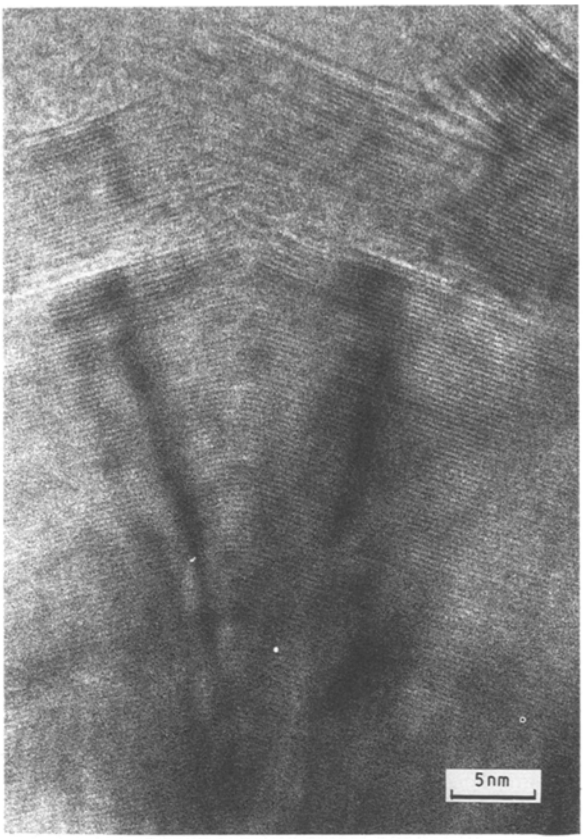

Figure 16 *in situ* (0 0 2) lattice image of a bent fibre.

region selected for the lattice image. For a fibre of such a relatively large size, about 1.5 μm, the lattice fringes are resolved to about 30 nm into the fibre. For finer fibres, this depth is improved to at least 50 nm. Lattice imaging is, therefore, available not only to probe the very surface structure, but also the layer organization more representative of the internal structure. Such (0 0 2) lattice images can be followed for several micrometres along the fibre edge with the Gatan TV system. Lattice fringes at the very edge are very disorganized: about three to four layers only are in register and disorientation is evident. The situation is very different beyond this layer: the coherent domain is at least 50 layers thick with very straight fringes. Disorientation manifest itself mostly in the form of a segmentation of the straight lattice domains. The directional change is generally associated with some lattice defect, like the dislocation and associated microvoid arrowed in Fig. 15.

Occasionally, more drastic defects were observed. Fig. 16 shows the edge region of a severely bent fibre. The stress field appears to be accommodated by the lattice inside the fibre by means of a continuous line of dislocations at the "elbow" of the bend. Towards the outside, however, presumably higher stresses have forced the lattice to split open. In Fig. 17, straight lattice lines are observed up to the very edge of the fibre but the outside layers appear to have been partly etched away in a periodic pattern, possibly as a result of oxidation.

Figure 18, finally, will be used to discuss further the question of the graphite grain morphology. The (0 0 2)

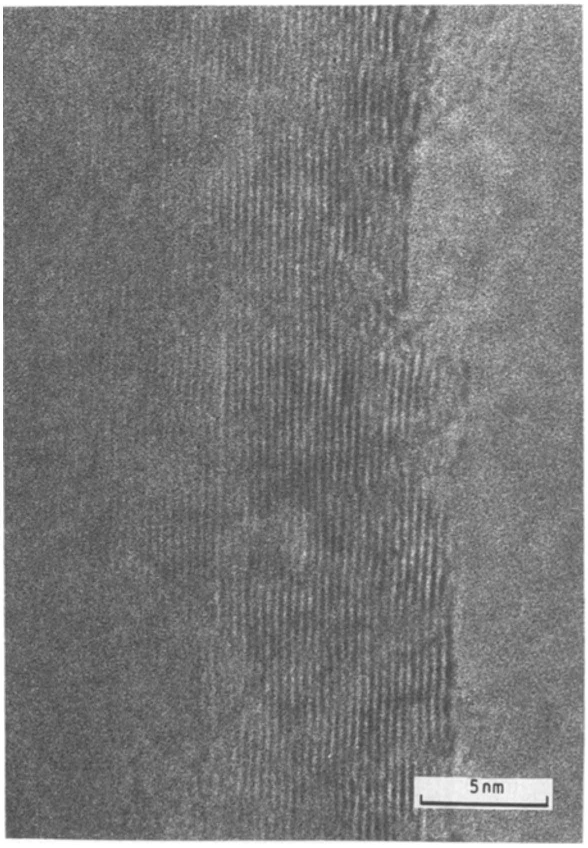

Figure 17 *in situ* (0 0 2) lattice image of a fibre edge showing surface etching.

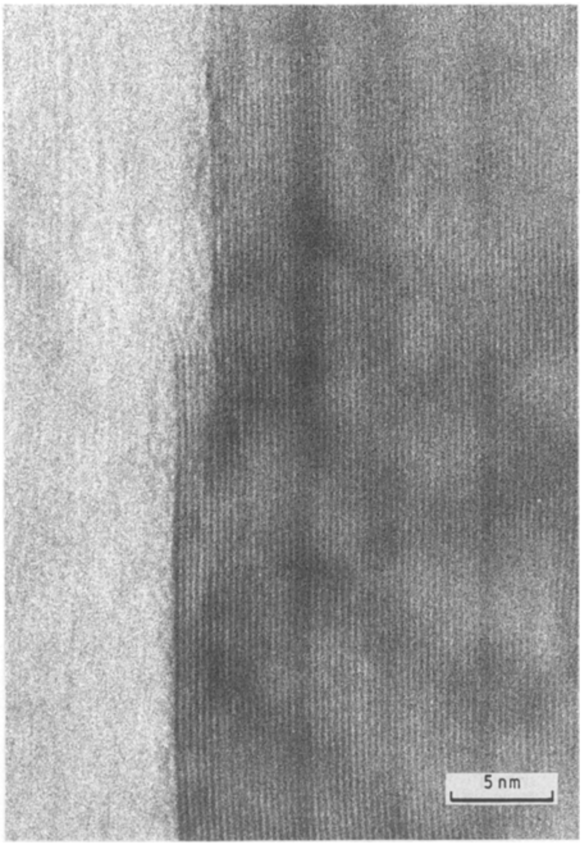

Figure 18 in situ (0 0 2) lattice image of a fibre edge displaying Bragg contours.

domain extends for at least 30 nm into the fibre. Most interesting in the picture are the Bragg contours (darker fringes). The narrow ones, elongated in the fibre direction, correspond to the dark striations of the brightfield images and may precisely delineate the graphite grains in (*h k l*) diffracting position. Other explanations of the contrast, like thickness variations or some type of lattice defect, are possible but investigation of these alternatives is beyond the scope of this work. If the former explanation holds, the lattice image provides the most accurate way of measuring the thickness of the graphite grains: regions of darker lattice lines encompass from 3 to 5 planes, i.e. 1 to 1.7 nm, which is in excellent agreement with the darkfield measurements.

5. Conclusion

The present study provides direct evidence for the graphitization of carbon fibres into a mosaic structure, in similar fashion to other man-made graphites [20], therefore supplying one of the last missing pieces in the description of carbon fibre structure. The graphite grains comprise a few atomic layers only, which probably explains why they escaped detection in previous investigations [12]: superposition effects are still overwhelming in the thinnest microtomed sections. Such effects have been avoided here through the availability of graphite whiskers with simple texture, allowing for artefact-free *in situ* characterization.

Past structure-property relationships studies have focused on the most important layer orientation and interaction parameters. Current understanding, as enounced by Johnson for example [23], is that limited layer plane stacking is essential for tensile strength. Implication of the mosaic structure in tensile as well as in compression failure deserves future attention. In particular, since graphitization appears restricted in highly folded textures [12], continuity of the mosaic into the folds of the sheet should be investigated. Aside from the mechanical properties issue, such TEM observation provides an ideal tool to characterize the highly planar textures desirable for high thermal and electrical conductivities. The *in situ* lattice imaging is also expected to provide valuable information concerning the various steps of the mesophase pitch spinning process and fibre post-treatments. Such investigations are in progress.

References

1. W. JOHNSON, in "Handbook of Composites", Vol. "1-Strong Fibers", edited by W. Watt and B. V. Perov, (North Holland, New York, 1985) pp. 389–443.
2. S. C. BENNETT, D. J. JOHNSON and W. JOHNSON, *J. Mat. Sci.* **18** (1983) 3337.
3. M. GUIGON, A. OBERLIN and G. DESARMOT, *Fibre Sci. Technol.* **20** (1984) 55.
4. D. J. JOHNSON, in "Chemistry and Physics of Carbon", Vol 20, edited by P. A. Thrower, (Marcel Dekker, New York, 1987) p. 1.
5. L. S. SINGER, US Patent 4 005 183 (1977).
6. *Idem, Carbon* **16** (1978) 408.
7. J. L. WHITE, in Proceedings of the Carbondale Conference, University of Illinois (1985).
8. H. HONDA, *Carbon* **26** (1988) 139.
9. D. A. SCHULZ, *SAMPE J.* March/April (1987), p. 27.
10. D. D. EDIE, N. K. FOX, B. C. BARNETT and C. C. FAIN, *Carbon* **24** (1986) 477.
11. H. SASAKI, T. SAWAKI and Y. YOSHIOKA, US Patent 4 628 001 (1986).
12. M. ENDO, *J. Mater. Sci* **23** (1988) 598.
13. E. J. ROCHE, J. G. LAVIN and R. G. PARRISH, *Carbon* **26** (1988) 911.
14. R. BACON, *J. Appl. Phys.* **31** (1960) 283.
15. J. V. SHARP and S. G. BURNAY, in Proceedings of the First Annual Conference on Carbon, London, 1971, p. 68.
16. B. RAND, in "Handbook of Composites", Vol. 1, edited by W. Watt and B. V. Perov (North Holland, New York, 1985) pp. 495–575.
17. J. C. H. SPENCE, in "Experimental High Resolution Electron Microscopy", (Clarendon Press, Oxford, 1981) p. 219.
18. S. C. BENNETT, D. J. JOHNSON and R. MURRAY, *Carbon* **14** (1976) 117.
19. G. R. MILLWARD and D. A. JEFFERSON, in "Chemistry and Physics of Carbon", Vol 14, edited by P. L. Walker and P. A. Thrower, (Marcel Dekker, New York, 1978) pp. 1–82.
20. A. OBERLIN, *Carbon* **17** (1979) 7.
21. P. A. THROWER, in "Chemistry and Physics of Carbon", Vol 5, edited by P. L. Walker, (Marcel Dekker, New York, 1969) p. 217.
22. A. MAUI and K. VIJAYAN, *J. Mater. Sci. Lett.* **6** (1987) 872.
23. D. J. JOHNSON, *J. Phys. D: Appl. Phys.* **20** (1987) 286.
24. W. RULAND and R. PLAETSCHKE, Extended abstracts of the 17th Biennal Conference on Carbon, Lexington (American Carbon Society, 1985) p. 356.
25. J. A. HUGO, V. A. PHILLIPS and B. W. ROBERTS, *Nature* **226** (1970) 144.
26. D. J. JOHNSON, *Phil. Trans. R. Soc. Lon.* **A294** (1980) 443.

Received 23 January
and accepted 16 August 1989